

Reradiation and Scattering from a Reconfigurable Intelligent Surface: a General Macroscopic Model

V. Degli-Esposti, *Senior Member, IEEE*, E. M. Vitucci, *Senior Member, IEEE*, M. Di Renzo, *Fellow, IEEE*, and S. Tretyakov, *Fellow, IEEE*

Abstract—Reconfigurable Intelligent Surfaces (RISs) have attracted attention in the last year for their characteristics of nearly-passive, thin structures that can dynamically change their reflection or refraction behaviour, and therefore realize anomalous reflection, focalization, or other wave transformations, to engineer complex propagation environments. Evaluating the performance and optimizing the deployment of RISs in wireless networks need physically sound frameworks that account for the actual physical characteristics of engineered metasurfaces. In this paper, we introduce a general macroscopic model for the realistic evaluation of RIS scattering, based on its decomposition into multiple scattering mechanisms and aimed at being embedded into ray models. Since state-of-the-art ray models can already efficiently simulate specular interactions (reflection, diffraction) and diffuse scattering, but not anomalous reradiation, we complement them with a Huygens principle approach and two possible implement. The different scattering mechanisms are combined through a generalization of the Effective Roughness model using a suitable power conservation equation. Notably, multiple reradiation modes can be modeled through the proposed approach. In addition, we validate the overall model's accuracy by benchmarking it against several case studies available in the literature, either based on analytical models, full-wave simulations, or experimental measurements.

Index Terms—Radio propagation, electromagnetic modeling, metasurfaces, ray tracing, reconfigurable intelligent surfaces.

I. INTRODUCTION

With the current deployment of fifth generation (5G) communication systems, it is now a critical time to identify enabling technologies for sixth generation (6G) wireless networks. 6G systems are expected to fulfill more stringent requirements than 5G systems, on transmission capacity, reliability, latency, coverage, energy consumption, and connection density. Existing 5G technologies, such as millimeter-wave communications, massive multiple-input multiple-output schemes, and ultra-dense heterogeneous networks, are mainly focused on the system design at the transmitter and receiver sides, as well as on the deployment of additional network infrastructure elements with power amplification, digital signal

processing capabilities, and backhaul availability. The purpose of currently available 5G technologies is mainly to cope with, or to capitalize on, often-unfavorable wireless propagation environments. In fact, the propagation environment has been conventionally modeled as an exogenous entity that cannot be controlled but can only be adapted to. According to this design paradigm, communication engineers usually design the transmitters, receivers, and transmission protocols based on the specific properties of the wireless channels and for achieving desired and target performance.

Recently, the technology referred to as reconfigurable intelligent surface (RIS) has emerged as a promising option for its capability of customizing the wireless propagation environment through nearly passive signal transformations. An RIS is a thin structure that is engineered to possess properties that enable the dynamic control of the electromagnetic waves through, e.g., signal reflections, refractions, focusing, collimation, and their combinations. In wireless communications, RISs are intended to realize so-called programmable and reconfigurable wireless propagation environments, i.e., wireless environments that are not viewed and treated as random uncontrollable entities but become part of the network design parameters that are subject to optimization, for supporting diverse performance metrics and quality of service needs and to fulfill the stringent requirements of 6G networks [1]–[4]. Recent applications of RISs in wireless communications include their use as nearly passive relay-type surfaces, signal-RF multi-stream multi-antenna transmitters, and reconfigurable ambient backscatters [5], [6].

An RIS is a new network element, to be deployed in future wireless networks, that is endowed with distinctive features and operation, usually without power amplification, regeneration, and signal processing capabilities [7]. An RIS operates, on the other hand, in the electromagnetic domain directly on the RF signals. Thanks to this peculiar mode of operation, the performance evaluation and optimization deployment of RISs in wireless networks require physically consistent and realistic models that account for their electromagnetic characteristics and physical implementation. For example, the analysis of the network coverage or spectral efficiency in RIS-assisted wireless networks require electromagnetically consistent models for the power scattered by the RISs as a function of their main parameters, which include the wave transformations that they apply, their size, their losses, their parasitic effects, and the transmission distance [5].

Manuscript received July XX, 2021; revised

(Corresponding author: Vittorio Degli-Esposti)

V. Degli-Esposti and E. M. Vitucci are with the Dept. of Electrical, Electronic and Information Engineering "G. Marconi", CNIT, University of Bologna, 40136 Bologna, Italy (e-mail: {v.deglesposti,enricomaria.vitucci}@unibo.it).

M. Di Renzo is with the Université Paris-Saclay, CNRS, CentraleSupélec, Laboratoire des Signaux et Systèmes, 91192 Gif-sur-Yvette, France (e-mail: marco.di-renzo@universite-paris-saclay.fr).

S. Tretyakov is with the Department of Electronics and Nanoengineering, School of Electrical Engineering, Aalto University, 02150 Espoo, Finland (e-mail: sergei.tretyakov@aalto.fi).

TABLE I: Summary of state-of-the-art contributions with their main features and limitations

Reference	Main features and limitations
[8]	<ul style="list-style-type: none"> - Physical optics methods and the scalar Huygens-Fresnel principle are used for analysis - Asymptotic scaling laws as a function of the transmission distance and the surface size are derived - Far-field and near-field case studies are considered and discussed - A two-dimensional space is considered
[9], [10]	<ul style="list-style-type: none"> - Antenna theory and a locally periodic (at the unit cell level) model for the surface are used for analysis - The model is validated with measurements using manufactured RIS (sub-6 GHz, millimeter-wave frequencies)
[11]	<ul style="list-style-type: none"> - Antenna theory is used for analysis - Far-field and near-field case studies are considered and discussed
[12]	<ul style="list-style-type: none"> - Surface antenna theory is used for analysis in the far-field region - Only the surface electric currents are included in the analysis
[13]	<ul style="list-style-type: none"> - Methods for electronically steerable parasitic array radiators are used for analysis - Scaling laws as a function of the transmission distance in the far-field and near-field are discussed
[14]	<ul style="list-style-type: none"> - Physical optics methods are used for analysis - The RIS is modeled as a multi-tile surface and each tile is a perfectly magnetic conductor - Each tile is modeled as an anomalous reflector and a scalable optimization algorithm is proposed
[15], [16], [17]	<ul style="list-style-type: none"> - A model based on impedance-controlled thin dipole antennas is proposed - The mutual coupling among the dipoles and the impact of the tuning elements are considered - Analytical and numerical optimization algorithms are introduced to exploit the mutual coupling
[18]	<ul style="list-style-type: none"> - Physical optics methods and the vector Huygens-Fresnel principle are used for analysis - Asymptotic scaling laws as a function of the transmission distance and the surface size are derived - Far-field and near-field case studies are considered and discussed - Multiple signal transformations are considered, including anomalous reflection and focusing - The surface can operate in reflection and refraction mode
[19]	<ul style="list-style-type: none"> - Physical optics methods and the vector Huygens-Fresnel principle are used for analysis - Phase-gradient surfaces that operate as anomalous reflectors are considered - A non-ideal multi-mode scattering model based on Floquet's theory is used for analysis
This paper	<ul style="list-style-type: none"> - Non-ideal scattering from a finite-size surface is considered - A parametric multi-mode scattering model based on a power flow conservation law is proposed - The scattering model accounts for specular reradiation, anomalous reradiation, and diffuse scattering - Two models based on the vector Huygens-Fresnel principle and antenna theory are analyzed and compared - The integration of the proposed multi-mode scattering model with ray tracing methods is discussed - The proposed model is tested and benchmarked against Floquet's theory, simulations, and empirical data

A. State-of-the-Art on Modeling Scattering from RISs

Motivated by these considerations, a few research works have recently investigated the scattering from finite-size RISs based on different analytical methods and modeling assumptions. A summary of the available contributions and a brief description of their main features and limitations can be found in Table I [8]–[19]. A more extensive state-of-the art review can be found in [18], [19].

Based on the analysis of Table I, we evince that, except for [18] and [19], the contributions available to date on modeling the scattering from finite-size RISs can be referred to as *ideal scattering models*. More precisely, the term “ideal” is referred to the assumptions that (i) the RIS is capable of scattering the incident radio waves towards a single specified direction (dominant) without generating parasitic scattered waves towards (unwanted) directions and (ii) the RIS is illuminated by a single plane wave that impinges upon its surface towards the single direction of design. Therefore, how an RIS would, e.g., scatter multipath components that are not considered in the design phase and the energy radiated towards parasitic modes are not explicitly considered. These two major assumptions can be removed by considering the analytical models proposed in [18] and [19], under some assumptions. In [18], Theorem 2 can be applied to any field E_S on the surface of the RIS, which can be even obtained from electromagnetic simulations and can account for multiple propagating modes. However, the subsequent analysis applied to reflective and refractive RISs is performed under the assumption that a single (the dominant) propagation mode exists. The analysis reported in

[19] explicitly accounts for the existence of multiple directions of reradiation based on Floquet's theory. This latter theory is, however, applicable only to periodic (e.g., phase-gradient) metasurfaces. Also, the main analysis is specialized to the far field of the RIS. Neither in [18] nor in [19], the authors consider the presence and impact of diffuse scattering that may be caused by, e.g., design tradeoffs, construction inaccuracies and dust or raindrops deposit. Furthermore, the scattering models proposed for RISs to date are based on either the Huygens-Fresnel principle under the physical optics approximation regime (e.g., [18], [19]) or antenna theory (e.g., [9], [10]). However, it is unclear to what extent these two methods can be applied and provide similar results. Based on these considerations, we evince that understanding and realistically modeling the scattering from finite-size RISs (realized either through periodical or aperiodical surfaces) that can apply general wave transformations is an open problem.

B. Proposed Methodology and Contributions

In contrast to the current state-of-the-art, in the present paper we introduce an approach for modeling scattering from a general finite-size, non-ideal RIS, that is conceived to be integrated into currently available ray-based models, such as Ray Tracing and Ray Launching, that are now recognized as the most suitable and efficient deterministic models for realistic radio propagation simulation in man-made environment. Given the important role that RISs will probably play in 6G - and beyond - systems, there is a need for reliable models that can simulate propagation in presence of both ordinary

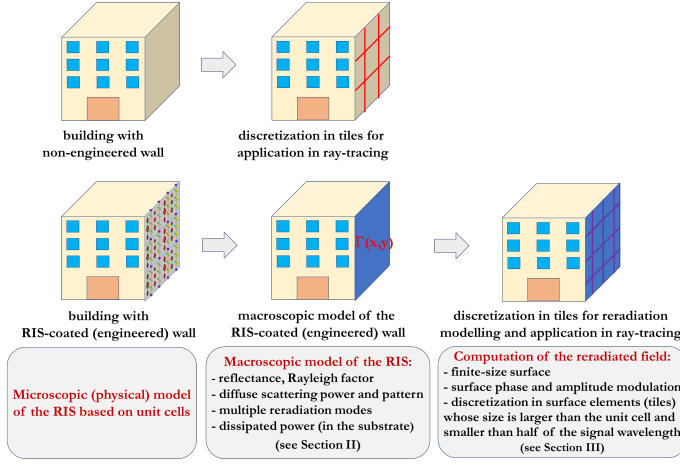


Fig. 1: Difference between non-engineered walls and RIS-coated walls: Proposed methodology and integration in ray-based models.

obstacles (e.g. terrain, buildings and vegetation) and artificially engineered objects such as RISs, to investigate the actual performance of future wireless systems.

Many ray-based models make use of the discretization of surfaces into surface elements (also called “tiles”) to simulate diffuse scattering (for instance using the Effective Roughness (ER) approach [20]) and to achieve good computational efficiency through parallel computing algorithms [21]. In the present work, we leverage this approach and the availability of parallel computing tools to simulate anomalous reflection (also referred to as anomalous reradiation in the following) using a method based on the Huygens-Fresnel (or simply Huygens) principle [22], as described in Sections II and III. In fact, a general ray-based approach to model anomalous reradiation is not available at the present time.

The methodology we propose to model RIS within a ray-based propagation simulator is sketched in Fig. 1. Ordinary walls are simply discretized to apply efficient ray-based models, then Geometrical Optics, Uniform Theory of diffraction and the ER model are applied to describe specular reflection, diffraction and diffuse scattering of the incident rays, respectively [21]. In contrast, RIS-coated walls are first homogenized and described through a proper reflection spatial modulation function $f(x,y)$ to compute anomalous reradiation, then discretized to apply a similar computation procedure as for ordinary walls.

Let’s now focus more specifically on scattering from RIS-coated walls, that will be the focus of the rest of this paper. Since RIS can also cause undesired specular reflection, diffraction and diffuse scattering in combination to anomalous reradiation, we decompose scattering from an RIS into three main scattering “macro-modes”:

- i) specular reflection/diffraction
- ii) diffuse scattering
- iii) anomalous reradiation

i) and ii) are computed using the well-established and efficient ray-based approach, while iii) is computed with the Huygens-based method described in Section III, but yet ex-

ploiting the same wall-discretization and parallel-computation framework. Eventually the three field contributions i)-iii) are summed coherently to get the overall scattered field. Key to the proposed method is the power-balance between the different contributions: this is achieved using a parameter-based approach and a proper power-balance equation to ensure that energy conservation is satisfied. Therefore, the proposed model for radiation and scattering from RISs is based on two steps.

- The first step defines and characterizes in terms of relative power of all possible scattering modes that are excited by the incident wave based on the physical implementation of the RIS, regardless of its finite size (see Section II). By enforcing a physically consistent conservation of the power flow, we define the power distribution among all the possible modes. This step is based on a generalization of the ER method [20], [21].
- The second step computes the field for each one of the scattering modes i)-iii) taking into account the finite size of the surface and its reradiation characteristics. Anomalous reradiation iii) is computed using two possible methods: A) the use of the Huygens-Fresnel principle based on a generalized version of the method of image currents [22], [23] (see Section III-A) and B) a simpler discrete implementation of the Huygens principle based on antenna theory that models the RIS as a planar array of antennas (Section III-B). Both methods use as an input the parameters obtained from the first modeling step, under the assumptions that the size of the RIS is large (but finite) compared to the wavelength.

Based on this methodology of analysis, the novelty and specific contributions of this paper are as follows:

- We introduce a general approach for modeling, in a parametric manner, scattering from a finite-size RIS that is suitable for integration into ray-based models.
- The proposed model is macroscopic as it is agnostic to the specific microscopic (unit cells) and physical implementation of the RIS, and it is instead characterized by macroscopic parameters. These parameters can be determined either through theoretical analysis (e.g., Floquet’s expansion for periodic surfaces) [19], through full-wave simulations, or through experimental measurements.
- The model explicitly takes into account diffuse scattering, in addition to desired and undesired reradiation modes.
- We consider and compare two different versions of the model for the computation of the anomalous reradiation field.
- The method makes use of a surface discretization, similarly to advanced discrete ray-based models [24] and can be therefore easily integrated into such models and parallelized on parallel computing platforms.
- The macroscopic scattering model is tested and validated against results available in the literature, which are based on theory, full-wave simulations, and measurements conducted on manufactured RISs. Results confirm the generality and accuracy of the proposed approach, as well as the non-negligible impact that multi-mode and

diffuse scattering may have on the total scattered field and, notably, on the far field radiation pattern of a finite-size RIS.

C. Paper Organization

The rest of this paper is organized as follows. In Section II, we introduce the first, power-balance step of the proposed macroscopic scattering model based on a power flow conservation principle. In Section III, we introduce and compare two methods for computing reradiated field from a finite-size RIS based. The integral formulation of the first method is fully explained in the Appendix. In Section IV, we validate the modeling approach introduced in Sections II and III with the aid of numerical simulations. Finally, Section V concludes this paper.

II. THE MACROSCOPIC SCATTERING MODEL FOR RISs

Even disregarding finite size and non-ideal, near field illumination, real-world metasurfaces do not attain ideal behaviour, i.e. they show multiple reradiation modes, although usually only one of them is the desired one. For example, considering anomalous reflectors conceived to reradiate a single plane wave toward a non-specular direction under plane wave illumination, only non-local designs do not generate parasitic modes, and only for a single incidence angle of design [25]. In common cases, such as periodic phase-gradient metasurfaces, specular reflection is one of the most relevant parasitic modes. In addition, diffuse scattering effects due to design tradeoffs, construction inaccuracies and dust or raindrops deposit on the surface can take place.

Since today's ray-based simulation tools are conceived to model specular reflection and diffuse scattering [21], but not anomalous reradiation, and since our objective is to include RIS simulation capabilities into ray-based simulators, we decided to develop the present RIS scattering model as a sort of plug-in extension of ray-based models. In addition, the proposed approach is conceived for several physical RIS implementations and wave transformations.

More precisely, the RIS is ideally assumed to be partitioned into surface elements of, in general, sub-wavelength size. This is compatible with ray-based models that use a tile-based discretization of ordinary surfaces. Surface discretization is necessary in particular for the discrete computation of the reradiated field, as discussed in section III. In general, the surface element does not correspond to a single unit cell of the RIS, or to any other element that characterizes the physical, microscopic implementation of the RIS.

Regardless of the discretization of the RIS, the first step of our proposed approach characterizes the RIS through a power-balance formulation, in terms a set of macroscopic parameters that provide the relative intensity of all scattering modes that are reradiated by the RIS towards different directions. The different reradiation modes can be obtained analytically from Floquet's theory in periodic, phase-gradient metasurfaces [19, Eq.(4)]. For general, non-periodic, RIS structures, the different modes and their corresponding amplitudes and phases, which depend on the angle of incidence and how the surface is

designed, can be obtained through full-wave simulations or measurements. In the proposed model we ignore the field reradiated by evanescent (non-propagating) modes. This implies that the approach is applicable to observation points at least a few wavelengths away from the surface of the RIS, where the impact of the evanescent modes can be safely assumed to be negligible. However, the proposed approach can be applied to both the near and far field of the RIS structure.

A. Modeling Principles

The proposed macroscopic model consists of two steps, as described in Section I-B: first the RIS is assumed to be of indefinite extent and a power balance between different scattering modes is applied, then its finite size and shape is taken into account for anomalous reradiation computation. The first step is described in this section, while the second step is discussed in Section III.

Power-balance is applied including into the equation specular reflection/diffraction, diffuse scattering and all the anomalous reradiation modes. The proposed approach is based on the ER model [20], [21], where a similar power balance was enforced between specular reflection and diffuse scattering only, which is here extended to account for anomalous reradiation. For this reason, we first briefly recall the original ER model.

B. The Effective Roughness Model

The ER model is an approach for modeling diffuse scattering from ordinary building walls in ray-based field prediction algorithms [20]. According to the ER model, a wall is split into surface elements that are often referred to as tiles. The size of the tiles is usually related to the angular discretization of the ray-based algorithm that is employed and to the distance between the source or the receiver and the tile. As illustrated in Fig. 2, the ER model is based on a power-flow conservation principle applied at the generic surface element (tile) of the wall. In Fig. 2, the generic tile is denoted by dS . A wave impinging on the tile is assumed to generate both a specular reflected wave and a diffuse scattered wave. In addition, some power penetrates into the material. The field scattered by each tile is modeled as a non-uniform spherical wave that departs from the tile itself and propagates in the same half space as the incident wave. The intensity of the scattered wave is determined by a scattering coefficient S and a scattering pattern that depend on the irregularities of the surface, as discussed next.

Based on Fig. 2, and assuming that the surface is illuminated by a wave of field \mathbf{E}_i from the direction of incidence θ_i , the following power flow conservation law holds:

$$P_i = P_r + P_s + P_p; P_i = \frac{|\mathbf{E}_i|^2}{2\eta} \cos(\theta_i) \quad (1)$$

where P_i , P_r , P_s , are the incident, specular reflected, and diffuse scattered power flows at the generic surface element dS , and P_p is the power that penetrates into the wall. More precisely, the model assumes that the wall has some surface or volumetric irregularities, with respect to an ideal uniform flat layer, that divert a fraction of power from specular reflection

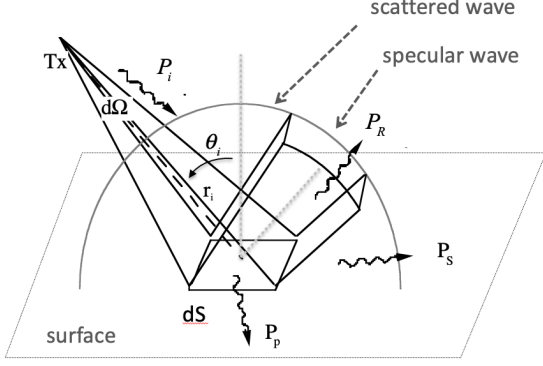


Fig. 2: Local power balance for the ER model: the incident power P_i is split into some specular reflected (P_r), diffuse (P_s) and transmitted (P_p) power.

towards other directions. The dissipated power P_p is assumed to be independent of the aforementioned irregularities.

Therefore, if we define the scattering parameter S ($0 < S < 1$) so that S^2 is the ratio of the diffuse scattering power to the reflected power and we use the specular field-reduction factor R (with $0 < R < 1$, often called Rayleigh factor) to account for reflection attenuation with respect to a smooth flat layer, from (1) we get:

$$P_i = R^2 \rho P_i + S^2 \rho P_i + P_p \quad (2)$$

where ρ is the wall's surface reflectance. If the wall were a perfectly smooth slab made of the same material as the wall under study, we would have:

$$P_i = \rho P_i + P_p \quad (3)$$

Combining (2) and (3), we shall see that the following identity needs to hold:

$$S^2 + R^2 = 1 \quad (4)$$

Eq. (4) makes evident that the higher the diffuse power, the lower the specular power and vice-versa.

Note that the foregoing power-balance can be considered global, i.e. valid for the whole surface area, if the transmitter is in the Fraunhofer far-field region of the surface: in this case the incident wave can be considered plane and the incidence angle can be assumed constant all over the surface.

After the power-balance step, the diffuse scattering field contribution is computed globally (far-field case) or for each tile (near-field case), according to a given scattering pattern, as explained in [20].

C. The Modified Effective Roughness Model for RISs

If a wall is coated with an RIS the wall turns into an engineered and reconfigurable surface, and the ER model needs to be generalized. In fact, RIS are designed to reradiate a properly transformed wave while minimizing specular reflection and diffuse scattering: therefore, anomalous reradiation needs to be included into the power-budget.

In the proposed macroscopic model, the reradiated wave is assumed to be generated through proper patterning (spatial

modulation of the reflector structure) along the surface of the RIS. However, the present approach is not intended to model the physical and microscopic operations at the surface, but the phase - and in some cases amplitude - spatial modulations of the incident fields that characterize anomalous reradiation, which are taken into account through the coefficients $\chi_m(x', y')$ (phase modulation) and $A_m(x', y')$ (amplitude modulation), respectively, see section III. In this section, however, we focus our attention on the overall redistribution of the incident power among all possible reradiation modes of the RIS (including specular reflection) and diffuse scattering, and not on their characteristics.

We consider, as for the original ER model, the power balance at the generic element dS .

For RIS-coated walls, the local power balance in (1) can be generalized as follows:

$$P_i = P_r + P_s + P_m + P_d \quad (5)$$

where the power that penetrates the RIS (P_p in (1)) is split into two contributions: P_m , the power reradiated by the RIS, and P_d , the power dissipated into the substrate of the RIS. As better described in Section III, each tile of the RIS is viewed as a secondary source of a set of reradiated spherical wavelets, and the superposition of the wavelets generated by the tiles yields the overall reradiated wave according to the Huygens' principle.

To determine reradiation, we introduce the reradiation intensity coefficient m , which gives the amount of incident power P_i that is reradiated into the anomalous reradiation mode. In simple terms, m plays for anomalous reradiation the same role that the reflectivity ρ plays for specular reflection. In RIS-coated walls, also, diffuse scattering may originate from, e.g., imperfections associated with the construction of the RIS, surface deviations from a perfect plane surface, and the deposit of dust on the surface and subtracts power from both specular reflection and anomalous reradiation in equal measure. Under these assumptions, from (5) we can write a power balance equation similar to (2):

$$P_i = R^2 \rho P_i + S^2 P_i + R^2 m P_i + \tau P_i \quad (6)$$

where the same notation as in (2) is used, with the caveat that the Rayleigh factor plays a role for both the specular and reradiated waves. In addition, the power dissipated in the substrate is conveniently expressed as a function of the incident power using the dissipation parameter τ . Moreover, we note that S^2 is redefined here as the ratio between the diffuse power and the incident power, instead of the reflected power.

Equivalently, (6) can be written as follows:

$$1 = R^2 \rho + S^2 + R^2 m + \tau \quad (7)$$

and, if the RIS is assumed to be perfectly flat and without imperfections (while still taking the power dissipated in the substrate into account), we obtain:

$$1 = \rho + m + \tau \quad (8)$$

Combining (7) and (8), the following identity needs to hold:

$$S^2 = (1 - R^2)(\rho + m) \quad (9)$$

Even though not explicitly stated in (6), it is important to mention that the triplet of parameters (ρ, m, τ) depends, in general, on the angle of incidence of the illuminating wave, i.e., $(\rho(\theta_i), m(\theta_i), \tau(\theta_i))$. If the RIS is illuminated by several waves from different directions, this implies that each signal needs to fulfill (6) based on the corresponding angle of incidence. In wireless communications, this scenario corresponds to a typical multipath propagation channel in which different incident multipath components are scattered by the RIS. In these cases, a complete angle-dependent characterization of the triplet $(\rho(\theta_i), m(\theta_i), \tau(\theta_i))$ is needed, which is usually obtained through full-wave numerical simulations or through measurements in an anechoic chamber. Notably, If the RIS is a periodic phase-gradient surface, the impact of the angle of incidence can be retrieved analytically by capitalizing on Floquet's theory [19, Eq. (4)].

As for the original ER model, in the far-field case, i.e. with a plane incident wave, the aforementioned parameters do not depend on the position of the considered dS on the surface, i.e. the power balance can be considered valid for the whole RIS. On the contrary, when the transmitter in the near-field with respect to the surface the incidence angle θ_i depends on the position: therefore the power balance has local validity and the macroscopic parameters must be considered function of position through θ_i . In case of metasurfaces with evanescent-waves (surface-waves, bound to the metasurface) that can transfer significant power between different areas of the RIS, we assume that the corresponding effect can be accounted for through the amplitude modulation coefficient $A_m(x', y')$ that will be introduced in Section III.

In (6), the reradiated power can be further expressed as a function of the ensemble of anomalous reradiation modes that are excited by the incident electromagnetic field and that are determined by the physical implementation and specific microstructure of the RIS. As an example, the authors of [25] have shown that a phase-gradient RIS that is engineered to operate as an anomalous reflector for a large deflection angle may reradiate power towards three dominant propagating modes: the direction of specular reflection, the desired direction of reradiation, and the direction symmetric to the nominal direction of reradiation.

Therefore, we assume that the RIS reradiates N dominant reradiated modes. By denoting with m_n the reradiation power coefficient of the n^{th} propagating mode, (7) and (9) can be re-written, respectively, as follows:

$$1 = R^2 \rho + S^2 + R^2 \sum_n m_n + \tau \quad (10)$$

and

$$S^2 = (1 - R^2) \left(\rho + \sum_n m_n \right) \quad (11)$$

where $\sum_n m_n$ can be interpreted as the (macroscopic) overall power reradiation coefficient of the RIS and the N -tuple (m_1, m_2, \dots, m_N) models how the reradiated power is distributed among the N modes.

Note that these N modes do not include the specular reflection mode that is accounted for separately, with the coefficient ρ . This is convenient because specular reflection

is usually the most significant of all parasitic diffracted modes and can be treated efficiently using the ray-based approach.

We note that the focus of this paper is the modeling and analysis of reflective surfaces, i.e., RISs that backscatter the incident signals. The proposed approach can be generalized for application to transmissive surfaces, i.e., RISs that scatter the incident signals towards the forward direction. In this case, the forward-ER scattering model can be applied [26], but this topic will be addressed in future work.

III. RERADIATED ELECTROMAGNETIC FIELD

The power flow conservation law in (10) ensures that every component that characterizes the electromagnetic field scattered from a finite-size RIS is consistently considered. In Section II, we have focused our attention only on the power conservation law among the possible sources of scattering from a finite-size RIS. In this section, we focus our attention on the field anomalously reradiated by the RIS and we discuss how to account for the spatial modulation along the surface (in phase and amplitude), which allows us to realize specified wave transformations.

As briefly described in Section II, each tile of a finite-size RIS is viewed as a secondary source of a spherical reradiated wavelet, with a given phase and intensity, and the superposition of the wavelets generated by the tiles that comprise the RIS provides the overall reradiated wave. As summarized in Table I, several methods have been proposed, each one having its own advantages, limitations, and assumptions, to calculate the field reradiated by a finite-size RIS. In the next two subsections, we propose two methods: (i) an integral formulation based on the induction equivalent [22] and on a generalized version of the method of image currents applied to RISs modeled as impedance sheets [5], [23]; and (ii) a method based on antenna theory. The two methods are compared against each other, in order to assess their applicability and performance.

Before introducing the two methods, we summarize in Algorithm I the overall proposed approach for computing the complete scattered field from a finite-size RIS, which encompasses the integration of one of the two reradiation models discussed in this section into ray-based models. More specifically: (i) the specular reflected field is obtained by using geometrical optics methods; (ii) the edge diffracted field related to the specular reflected field is obtained by applying the uniform theory of diffraction [21]; (iii) the diffuse scattering is obtained from the ER model introduced in Section II-B and (iv) the reradiated field is obtained through the methods described in section III.A or III.B. The first three contributions are already available in conventional ray-based simulators, which can then be used in Algorithm I provided that the power flow conservation law (10) is fulfilled. As mentioned, the focus of the rest of this section is, on the other hand, the computation of the reradiated field, which is not available in current ray-based simulators.

A. Reradiated Field Computation Method Based on an Integral Formulation

The first method used to derive the reradiated field is an integral formulation based on the application of the induction

Algorithm I: Computation of the RIS-scattered total field
1. Electromagnetic characterization of the RIS (via analysis, full-wave simulations, or measurements). For every reradiation mode, the parameters (ρ, m_n, S, τ) are defined as a function of the angle of illumination. In this step, the RIS is assumed to be of undefined extent, no tiling is needed, except for non-local metasurfaces.
2. Computation of the field due to specular reflection: E_{specular} based on geometrical optics [21].
3. Computation of the diffracted field from RIS edges related to specular reflection: $E_{\text{UTD-diffraction}}$. This is obtained through ray-based models that use, e.g., the uniform theory of diffraction [21].
4. Computation of the field due to diffuse scattering: E_{diffuse} . This is obtained through the ER model introduced in Section II-B, which is already available in ray-based simulators [21].
5. Computation of the field reradiated by the RIS: E_m . This is obtained through the method introduced in Section III-A (see (16)) or in Section III-B (see (26) and (31)).
6. Computation of the total scattered field through coherent summation: $E_{\text{RIS}} = E_{\text{specular}} + E_{\text{UTD-diffraction}} + E_{\text{diffuse}} + E_m$

Algorithm I - Proposed approach for modeling the total scattering from a finite-size RIS and its integration into ray-based models and simulators.

theorem [22], [23] and on a generalized version of the method of image currents. The essence of the proposed method consists of replacing the physical structure of the RIS with equivalent (surface) electric and magnetic current densities, which are assumed to radiate in the absence of the RIS. The equivalent surface current densities allow us to compute the electromagnetic field reradiated by the RIS.

To this end, we first introduce the following macroscopic reflection coefficient:

$$\Gamma(x', y') = R \cdot \sqrt{m} \cdot A_m(x', y') \exp(j\chi_m(x', y')) \quad (12)$$

where $P' = (x', y') \in S_{\text{RIS}}$ is a generic point of the surface of the RIS, S_{RIS} . As introduced in Section II, m is the reradiation intensity coefficient, and R is the Rayleigh coefficient which accounts for reradiation attenuation caused by diffuse scattering. On the other hand, $A_m(x', y')$ and $\chi_m(x', y')$ are the amplitude and phase of the spatial modulation introduced by the RIS to realize the desired wave transformations, e.g., anomalous reflection or focusing. To ensure that the power conservation flow in (7) is fulfilled, we assume:

$$\int_{S_{\text{RIS}}} A_m^2(P') dP' = 1$$

In the case of a locally-designed phase-gradient RIS, which allows the propagation of more than one reradiation mode, eq. (12) can be rewritten in the following form: $\Gamma(x', y') = R \cdot \sum_{n=1}^N \sqrt{m_n} \cdot \exp(j\chi_{m_n}(x', y'))$, where N is the number of reradiation modes, and m_n, χ_{m_n} are the reradiation intensity coefficient, and the phase modulation coefficient of the n^{th} propagating mode, respectively, while the amplitude modulation coefficient is a unitary constant in this case.

The surface reflection coefficient in (12) needs to be interpreted as a macroscopic spatial modulation applied to the incident signal. In other words, $\Gamma(x', y')$ is actually determined by the actual microscopic structure and phenomena taking place on the RIS, but it conveniently summarizes and bypasses them for the sake of simply representing their final effects on the reradiated wavefront. Let us assume that the macroscopic

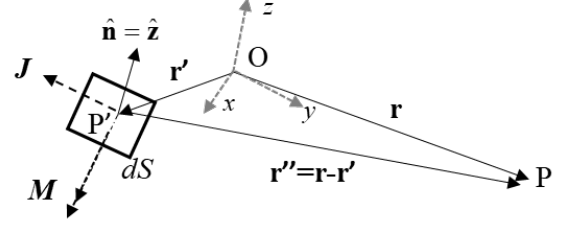


Fig. 3: Generalized current source that corresponds to a generic surface element dS .

model of the RIS exemplified by $\Gamma(x', y')$ in (12) is known, e.g., through some analytical models, full-wave simulations, or measurements. Let us adopt the notation illustrated in Fig. 3 for a generic surface element (dS) of the RIS, where P is the observation point where the electromagnetic field needs to be evaluated. More specifically, we consider a finite-size RIS that lies in the $xy(z=0)$ plane of an $Oxyz$ coordinate system. The generic surface element is denoted by dS and is centered at the point $P' = (x', y') \in S_{\text{RIS}}$, and $\hat{\mathbf{n}}$ is the normal unit vector that points outwards (i.e., towards the reflection half-space) the surface element dS .

In order to derive the reradiated field by the RIS in the upper half space identified by $\hat{\mathbf{n}}$ (i.e. the reflection half-space), the induction theorem is applied [22], [23]: the original electromagnetic scattering problem is turned into an equivalent problem (“induction equivalent”), where the sources of the incident field are removed, and a distribution of electric and magnetic current densities, which are the (equivalent) sources of the reradiated field, is impressed on the RIS surface.

In conventional electromagnetic scattering problems, the induction equivalent problem is solved for those surfaces that can be modelled as PEC or PMC by removing the surface and applying the method of image currents, and then computing the total surface current densities, which are magnetic-only or electric-only, respectively. After that, the reradiated field is computed by using radiation integrals in the homogenized medium. However, this approach is not directly applicable to engineered surfaces like an RIS is. An RIS can be viewed, in fact, as a layer with a generic surface impedance as illustrated in [18], [27], and requires both electric and magnetic surface currents to co-exist simultaneously. Therefore, the method of images needs to be generalized, as explained in Appendix A.

Following this approach, the field reradiated by an RIS can be thought of as generated by the following surface electric (\mathbf{J}) and magnetic (\mathbf{M}) current densities, which depend on the incident fields and on the macroscopic surface reflection coefficient Γ (see Appendix A):

$$\begin{aligned} \mathbf{J}(P') &= (1 + \Gamma(P')) [\mathbf{H}_{it}(P') \times \hat{\mathbf{n}}] \\ \mathbf{M}(P') &= (1 - \Gamma(P')) [\hat{\mathbf{n}} \times \mathbf{E}_{it}(P')] \end{aligned} \quad (13)$$

where $(P' = (x', y') \in S_{\text{RIS}})$, and \mathbf{E}_{it} , \mathbf{H}_{it} denote the tangential components of the incident electric and magnetic fields evaluated on the surface of the RIS, respectively. If the RIS reduces to a conventional PEC (i.e., $\Gamma = -1$) we obtain, as expected, $\mathbf{J}(P') = 0$ in (13), as the induced electric currents

are shorted by the PEC surface. Similarly, for a conventional PMC (i.e., $\Gamma = 1$), we get $\mathbf{M}(P') = 0$.

In other words, with the proposed method the RIS is first assumed to be of infinite extent, and it is modeled through equivalent surface electric and magnetic currents: in particular, each surface element dS is viewed as an infinitesimally small part of a sheet of induced (equivalent) electric and magnetic currents, which are determined by the incident field and by $\Gamma(P')$ in (12) for $P' = (x', y') \in S_{RIS}$.

Then, the reradiated field is computed by using radiation integrals, which account for the finite size and the shape of the RIS – and then allows computation of the overall reradiated field, including the diffracted field related to anomalous reradiation – as if the RIS were absent.

With this approach anyway we do not consider that the surface currents are discontinuous at the edges of the RIS, and this implies that the expression of the reradiated field are approximated, as we neglect the perturbation effect on the field caused by these discontinuities. This is, however, a good approximation if the size of the RIS is large compared with the signal wavelength and if the spatial variations of the surface currents are sufficiently slow at the scale of the RIS microstructure.

The finite size of the RIS is taken into account next by considering the radiation integrals. To this end, without loss of generality, we assume that the incident signal is a far-field (with respect to the transmitter) spherical wave whose electric and magnetic fields can be formulated as follows:

$$\begin{aligned} \mathbf{E}_i &= \sqrt{\frac{\eta}{2\pi}} P_t G_t \cdot e^{j\chi_0} \cdot \frac{e^{-jkr_i}}{r} \hat{\mathbf{p}}_i \\ \mathbf{H}_i &= \frac{1}{\eta} \hat{\mathbf{k}}_i \times \mathbf{E}_i \end{aligned} \quad (14)$$

where η is the free-space impedance, P_t and G_t are the radiated power and the antenna gain of the transmitter, respectively, $\hat{\mathbf{p}}_i$ is a unit-norm vector that embodies the polarization of the incident wave, $\hat{\mathbf{k}}_i$ is the propagation vector, $k = 2\pi/\lambda$ is the wave number, χ_0 is a fixed phase shift, and “ \cdot ” denotes the vector product. Also, r_i is the distance from the (center) of the transmitter to the point where the fields are computed. If the fields are observed on the surface of the RIS, then $r_i = r_i(P')$.

From (14), the tangential fields \mathbf{E}_{ir} and \mathbf{H}_{ir} in (13) can be formulated, by definition, as follows:

$$\begin{aligned} \mathbf{E}_{ir}(P') &= \hat{\mathbf{n}} \times \mathbf{E}_i(P') \times \hat{\mathbf{n}} \\ \mathbf{H}_{ir}(P') &= \hat{\mathbf{n}} \times \mathbf{H}_i(P') \times \hat{\mathbf{n}} \end{aligned} \quad (15)$$

As illustrated in Fig. 3, let $\mathbf{r}' = (x', y', z' = 0)$ denote the coordinates of the generic point P' of the RIS, let $\mathbf{r} = (x, y, z)$ denote the coordinates of the observation point P whose corresponding unit-norm vector is $\hat{\mathbf{r}}$, and let define the difference vector $\mathbf{r}'' = \mathbf{r} - \mathbf{r}'$. Assuming for simplicity that the RIS does not change polarization of the incident wave, the electric field reradiated by the RIS can be formulated (the analytical details

are available in Appendix A) as follows:

$$\begin{aligned} \mathbf{E}_m(P) &= \iint_{S_{RIS}} j \frac{e^{-jkr''}}{\lambda r''} [\hat{\mathbf{r}}'' \times (\eta \hat{\mathbf{n}} \times \mathbf{H}_a(x', y')) \times \hat{\mathbf{r}}''] dS \\ &+ \iint_{S_{RIS}} j \frac{e^{-jkr''}}{\lambda r''} [\hat{\mathbf{r}}'' \times (\mathbf{E}_a(x', y') \times \hat{\mathbf{n}})] dS \end{aligned} \quad (16)$$

where $r'' = |\mathbf{r}''|$, $\hat{\mathbf{r}}'' = \mathbf{r}''/|\mathbf{r}''|$, and the following (surface) electric and magnetic fields are defined:

$$\begin{aligned} \mathbf{E}_a(P') &= -(1 - \Gamma(P'))/2 \mathbf{E}_{ir}(P') \\ \mathbf{H}_a(P') &= (1 + \Gamma(P'))/2 \mathbf{H}_{ir}(P') \end{aligned} \quad (17)$$

The fields in (17) can be interpreted as an *RIS-modified Huygens's field source*, which is completely determined by the tangential components of the incident waves and by the macroscopic amplitude reflection coefficient in (12). In the reference case of a PEC surface (i.e. $\Gamma = -1$), the first of (17) becomes $\mathbf{E}_a = -\mathbf{E}_{ir}$, so that the total tangential electric field on the surface is zero, as it should be in this case.

It is worth noting that according to the induction theorem (16) gives a valid result only if the reradiated field is computed in the half space above the surface (i.e. if P belongs to the reflection half space). Moreover, due to the approximations used in its derivation, (see eq. (A.6) in Appendix A), (16) is valid if P belongs to far field or to the radiative near field region of the RIS, but not to the reactive field region: from a practical point of view, it is enough that P is located at a distance of few wavelengths from the RIS surface.

The reradiated magnetic field \mathbf{H}_m can be obtained in a similar way, by computing the radiation integral for magnetic field.

The present formulation may be generalized to RISs that change the polarization of the incident wave.

Simplified, closed-form expressions for (16) can be obtained in the Fraunhofer far field region of the RIS [18], [19] (see Appendix A). In this paper we employ (16), since in many practical applications the RIS can be large and then the observation P point may fall in the radiative near-field region. However, in such a case (16) cannot be solved in closed form and must be computed numerically, by properly discretizing the RIS surface.

B. Reradiated Field Computation Method Based on Antenna Theory: Antenna Array-Like Model

Based on (16), the field reradiated by a finite-size RIS can be obtained by computing a finite integral. The accuracy of the computation depends on the discretization of the integral with the only constraint that the quantization step needs to be less than half of the wavelength λ : assuming equal quantization in both x and y directions it must be $dS < (\lambda/2)(\lambda/2) = \lambda^2/4$, for ensuring an appropriate spatial sampling without causing grating lobes [18]. We clarify that this discretization is just needed for the numerical calculation of (16) and it is not directly related to the microscopic implementation of the RIS, i.e., the size of the unit cells. The numerical calculation of (16) for a single RIS poses, in general, no problem. If, however, (16) is employed to analyze system performance,

e.g., to estimate the coverage maps of a large-scale geographic region in which multiple RISs are used, the computational burden may not be negligible. The issue may be solved, in part, by using parallelized implementations that exploit high performance graphic processing units that may provide a good computation efficiency [24]. However, it is important to analyze other possible methods that may be used in lieu of (16) to further reduce computational burden as well as formulation complexity.

In the recent literature, another approach that has been used for estimating the field reradiated by a finite-size RIS is based on antenna theory, according to which an RIS is viewed as an array of reflecting antenna elements [9]–[11]. Based on this approach, the RIS is subdivided into surface elements of area ΔS , and each surface element can be thought of as an antenna that receives the incident power (P_i) and reradiates a spherical wavelet of power (P_m) (as defined in (5)) according to a given radiation pattern $f_m(\theta_m)$, where θ_m is the angle of observation of the reradiated wave, that needs to be appropriately chosen. It is worth mentioning that the finite surface element ΔS needs not to be confused with the infinitesimal area dS used in (16), since the approach described in this section is conceptually different. Even here, ΔS is a theoretical surface element that doesn't have any relationship with the physical microstructure of the RIS. In the following, we elaborate on the constraints that ΔS needs to fulfill for ensuring that the Antenna Array-Like (AAL) model is physically sound.

1) *General considerations*: the representation of a finite-size RIS as an antenna array is based on the concept of duality of an antenna in transmission and reception, and, more precisely, on the well-known relation between the effective aperture (A_m) and the directivity (D_m) of an antenna, i.e., $D_m = (4\pi/\lambda^2) A_m$ [23].

If we consider ΔS as an aperture antenna, the antenna effective aperture needs not to be greater than the physical aperture size, i.e., $A_m \leq \Delta S$, otherwise the antenna could receive and reradiate more power than the power entering its aperture (i.e., $P_m > P_i$), thus violating the principle of energy conservation. Therefore, it must be pointed out that if the antenna aperture tends to zero (or at least becomes electrically small, $\Delta S \ll \lambda$), the foregoing relation between D_m and A_m does not hold true anymore as the directivity of an aperture antenna cannot be lower than 3 [28]. For thin radiating elements, such as short dipole antennas, there exists no simple relationship between their physical size and their effective area. However, if such dipoles are densely cast into a planar array, mutual coupling effects need to be taken into account for ensuring that the principle of energy conservation is fulfilled, which results in the failure of the mentioned relation between D_m and A_m , similarly to the foregoing case of aperture antennas [15].

In order to formulate the AAL model presented in this paper we consider antenna elements for which all the following physical relations are supposed to be true:

$$\begin{cases} D_m = (4\pi/\lambda^2) A_m \\ A_m \leq \Delta S \\ \Delta S \leq \lambda^2/4 \end{cases} \Rightarrow D_m \leq \pi \quad (18)$$

where the third inequality ensures the absence of grating lobes. For ease of notation, we denote $\Delta S = (\Delta l)^2$, which yields $\Delta l \leq \lambda/2$ and $\Delta l = \delta \lambda$ with $\delta \leq \delta_{max} = 1/2$. Then, from (18), we obtain:

$$\begin{aligned} D_m &= (4\pi/\lambda^2) A_m \leq (4\pi/\lambda^2) \Delta S \\ &= 4\pi (\Delta l/\lambda)^2 = 4\pi \delta^2 \end{aligned} \quad (19)$$

By definition, directivity D_m is always greater than one, which, from (19), implies:

$$\begin{aligned} 4\pi \delta^2 &\geq D_m \geq 1 \\ \Rightarrow \delta &\geq \delta_{min} = 1/(2\sqrt{\pi}) \approx 0.28 \end{aligned}$$

Therefore, δ must satisfy the following constraint:

$$0.28 = \delta_{min} \leq \delta \leq \delta_{max} = 0.5 \quad (20)$$

From the lower bound in (20) we evince that the representation (modeling) of a finite-size RIS as an array of antenna elements can be considered sound if the size of each antenna element is larger than $\Delta l_{min} = 0.28\lambda$. This limitation was recently found through experimental measurements in [9] and [10], where the Authors identified a lower limit to the size of the surface element, that was assumed there coincident with a unit cell of the RIS, and reckoned that a proper radiation pattern needed to be chosen as a function of the size of the unit cell in order to obtain physically consistent and accurate results. It is also worth mentioning that mutual coupling among the antenna elements cannot be ignored if $\Delta l < \lambda/2$ and that it can be approximately taken into account by applying periodic boundary conditions when estimating the reflection coefficient of each unit cell [9], [10], [20].

One antenna pattern often utilized in the literature is the exponential-Lambertian pattern (see, e.g., [9], [10]). In this case, the power radiation pattern is the following:

$$f_m(\theta_m) = (\cos \theta_m)^\alpha, \quad \theta_m \in [0, \pi/2] \quad (21)$$

where $\alpha \geq 0$ is a tuning parameter.

By definition of directivity, from (21) we obtain ([10], Eq. (16)) $D_m = 2(\alpha + 1)$. From (18), we get (for every value of δ):

$$D_m = 2(\alpha + 1) \leq \pi \Rightarrow \alpha \leq \frac{\pi}{2} - 1 \approx 0.57 \quad (22)$$

Larger values of α would result in grating lobes. Since, in addition, $\alpha \geq 0$, from (19) it must be:

$$4\pi \delta^2 \geq 2(\alpha + 1)|_{\alpha=0} \Rightarrow \delta \geq 1/\sqrt{2\pi} \approx 0.4 \quad (23)$$

Considering (22), (23) and (20), radiation pattern (21) can be employed for modeling a RIS only if $0.4 \leq \delta \leq 0.5$ and $\alpha \leq 0.57$. In particular, if the surface element is assumed equal to the RIS' unit cell as in [9], [10], the exponential-Lambertian radiation pattern cannot be used for RISs whose unit cells are electrically small.

The antenna pattern we choose as the reference in the present work for the AAL model is the Huygens source radiation pattern. The Huygens source represents the reference small aperture antenna and therefore can be used for a discrete implementation of the Huygens principle [28]. The Huygens power radiation pattern is:

$$f_m(\theta_m) = ((1 + \cos \theta_m)/2)^2, \quad \theta_m \in [0, \pi] \quad (24)$$

By definition of directivity from (24) we easily get $D_m=3$.

Therefore from (19), we get:

$$4\pi\delta^2 \geq D_m = 3 \Rightarrow \delta \geq \frac{1}{2} \sqrt{\frac{3}{\pi}} \simeq 0.49 \quad (25)$$

Equation (25) means that the use of a Huygens radiation pattern in the AAL model is only compatible with antenna spacings greater or equal to 0.49λ .

2) *Reradiated field computation*: under the assumption that feasibility conditions in (18)-(20) are fulfilled we are in the position to formulate the field reradiated by the RIS as the sum of the far-field spherical wavelets (i.e. at a distance of at least 10λ from ΔS) reradiated by each surface element. The RIS is partitioned into $N_X \times N_Y$ elementary surface elements, the generic surface element is denoted by the indices (u, v) , where $u = 1, 2, \dots, N_X$ and $v = 1, 2, \dots, N_Y$, and its reradiated electric field contribution is denoted by $\Delta \mathbf{E}_m(u, v)$. Then, the RIS-reradiated field at the observation point P is formulated as:

$$\mathbf{E}_m(P) = \sum_{u=1}^{N_X} \sum_{v=1}^{N_Y} \Delta \mathbf{E}_m(P|u, v) \quad (26)$$

To compute $\Delta \mathbf{E}_m(u, v)$, we use a two-step approach: (i) first, we ensure that the reradiated power fulfills the power flow conservation law in (7) or (10) then, we account for the phase and polarization modulation that each surface element ΔS needs to apply in order to realize the desired wave transformation.

For what concerns power conservation, it is enforced by the power balance formulated in Section II-C between the model's parameters m, τ, ρ, S . Therefore, we must assume the antenna elements of the AAL model to be ideal, i.e. all the power impinging on their area ΔS must be received, since non-idealities and losses are taken into account in the cited power balance by the fact that $m \leq 1$. As a consequence, we assume $A_m = \Delta S$. In case of Huygens antenna elements, we will therefore consider the equal sign in equation (25) and thus an array spacing $\Delta l = 0.49\lambda$, which satisfies all the feasibility conditions and also the condition for negligible antenna coupling.

We denote by $\theta_i(u, v)$ and $\theta_m(u, v)$ the angle of the incident wave and the angle of the reradiated wavelet that correspond to the surface element (u, v) , respectively. The reradiated electric field can be formulated as follows:

$$\Delta \mathbf{E}_m(P|u, v) = \Delta E_{m0}(P|u, v) \sqrt{f_m(\theta_m(P|u, v))} \times \Gamma(u, v) \exp(-jk(r_i(u, v) + r_m(P|u, v))) \hat{\mathbf{p}}_m \quad (27)$$

where $\hat{\mathbf{p}}_m$ is a unit-norm vector that embodies the polarization of the reradiated wave, $\Delta E_{m0}(P|u, v)$ is the complex amplitude of the reradiated wave, $\Gamma(u, v)$ is the macroscopic reflection coefficient in (12) evaluated at $(x', y') = (\Delta l u, \Delta l v)$, and the exponential term accounts for the accumulated phase shift of the path-length from the transmitter to the (u, v) th surface element of the RIS and from the latter surface element to the receiver, which depends on the corresponding distances $r_i(u, v)$ and $r_m(P|u, v)$, respectively. In (27), we have made explicit that the angle of the reradiated wave depends on the observation point P .

In order to ensure that a fraction equal to mR^2 of the power received by the antenna element is reradiated in the upper half-space (a solid angle of 2π steradians), therefore fulfilling the power conservation law, the following power-balance equation needs to hold:

$$\begin{aligned} mR^2 \frac{|\mathbf{E}_i|^2}{2\eta} A_m(\theta_i) &= mR^2 \frac{|\mathbf{E}_i|^2}{2\eta} \frac{\lambda^2}{4\pi} f_m(\theta_i) = \\ &= \int_{2\pi} \frac{|\Delta \mathbf{E}_m(P)|^2}{2\eta} r_m^2 d\Omega = 2\pi \frac{|\Delta E_{m0}(P)|^2}{2\eta} \\ &\quad \times \int_0^{\pi/2} f_m(\theta_m) r_m^2(P|u, v) \sin(\theta_m) d\theta_m \end{aligned}$$

where the indications of the dependence on (u, v) have been temporarily dropped for the sake of simplicity. Therefore, we get:

$$\begin{aligned} mR^2 |\mathbf{E}_i|^2 \frac{\lambda^2}{4\pi} f_m(\theta_i) &= 2\pi |\Delta E_{m0}(P)|^2 \\ &\quad \times \int_0^{\pi/2} f_m(\theta_m) r_m^2(P) \sin(\theta_m) d\theta_m \end{aligned} \quad (28)$$

where $|\mathbf{E}_i|^2 = \eta/2\pi \times P_i G_i / r_i^2(u, v) = E_{i1}/r_i^2(u, v)$ is the incident electric field intensity according to (14).

Therefore, the total reradiated field intensity can be formulated as follows :

$$|\Delta E_{m0}(P)|^2 = \frac{\lambda^2}{8\pi^2} \frac{mR^2 E_{i1}}{\int_0^{\pi/2} f_m(\theta_m) \sin(\theta_m) d\theta_m} \frac{f_m(\theta_i)}{r_i^2 r_m^2} \quad (29)$$

By combining (27) and (29), the reradiated electric field expression can be derived:

$$\begin{aligned} \Delta \mathbf{E}_m(P|u, v) &= \frac{\lambda}{2\pi} \frac{\sqrt{mR} E_{i1}}{\sqrt{2 \int_0^{\pi/2} f_m(\theta_m) \sin(\theta_m) d\theta_m}} \Gamma(u, v) \hat{\mathbf{p}}_m \\ &\quad \times \sqrt{f_m(\theta_i(u, v))} \sqrt{f_m(\theta_m(P|u, v))} \\ &\quad \times \frac{\exp(-jk(r_i(u, v) + r_m(P|u, v)))}{r_i(u, v) r_m(P|u, v)} \end{aligned} \quad (30)$$

The far-field magnetic field contribution of the generic surface element can be easily computed using the well known local plane wave relation:

$$\Delta \mathbf{H}_m = (1/\eta) \hat{\mathbf{r}}_m \times \mathbf{E}_i$$

Using (30), the overall reradiated electric field can be obtained from (26). It is worth noting that expression (30) satisfies reciprocity as it is invariant with respect to the exchange of (θ_i, r_i) for (θ_m, r_m) .

In case of a Huygens radiation pattern, the integral can be easily solved to get:

$$\begin{aligned} \Delta \mathbf{E}_m(P|u, v) &= \sqrt{mR} E_{i1} \Gamma_m(u, v) \hat{\mathbf{p}}_m \\ &\quad \times \frac{3\lambda}{16\pi} (1 + \cos \theta_i(u, v)) (1 + \cos \theta_m(P|u, v)) \\ &\quad \times \frac{\exp(-jk(r_i(u, v) + r_m(P|u, v)))}{r_i(u, v) r_m(P|u, v)} \end{aligned} \quad (31)$$

Equation (31) has been used in the following section when validating the AAL model.

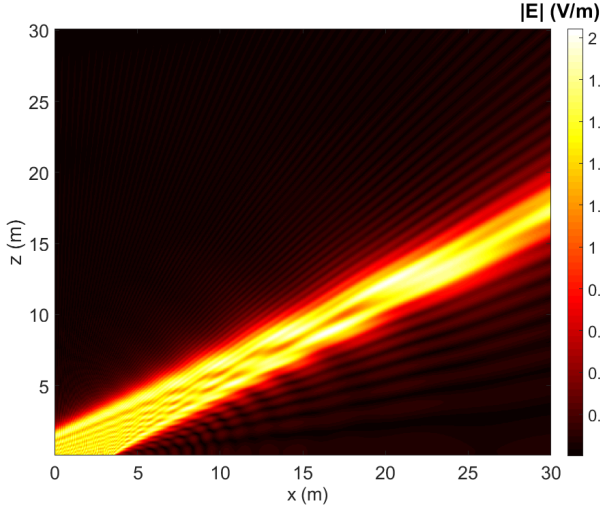


Fig. 4: Reradiated field [V/m] in the xz plane for a 7×7 m horizontal RIS (in the xy plane) centered in the origin. Setup: 3 GHz operating frequency, normal incidence, reflection towards an angle of 60 degrees.

IV. MODEL VALIDATION

In this section, we validate the proposed macroscopic model for RISs by testing it against several reference types of metasurface available in the literature, based on electromagnetic simulations and/or experimental measurements. The objective of this section is to show that the proposed model can be employed to simulate several practical metasurfaces, including non-ideal phenomena and illumination conditions. Six case studies are analyzed.

1) *Ideal Anomalous Reflector*: the first case study corresponds to an ideal metasurface designed to reradiate a single plane-wave mode towards the desired direction and in absence of dissipation or any other reradiation mode. It is worth noting that, although we necessarily model this case with a local, phase-gradient approach, only non-local metasurfaces can realize an ideal lossless anomalous reflector [25]. We consider a 7×7 m large RIS that lies in the xy plane and a generalized reflection law phase profile [25] $d\chi_m(x')/dx' = k(\sin\theta_i - \sin\theta_r)$ in (12), where θ_i is the angle of incidence and θ_r is the desired angle of reflection. The RIS is illuminated normally ($\theta_i = 0$) by a 3 GHz plane wave with a linear polarization in the y -direction and intensity 1 V/m. The angle of reradiation is assumed to be $\theta_r = 60$ degrees. The reradiated field computed with the integral version of the model (section III-A) is reported in Fig. 4.

In Fig. 4, the considered distances lie in the near field region of the RIS, since the Fraunhofer far field of the whole metasurface is approximately equal to 1000 m. We observe that the field is steered towards the desired angle of reflection. As expected, in addition, we observe edge-diffraction fringes that are due to the finite size of the RIS.

For comparison, we compute the reradiated field by using the AAL formulation of the model (equations (26) and (31)). For fairness, (16) is computed by using the same discretization as (26). The comparison is illustrated in Fig. 5 where the

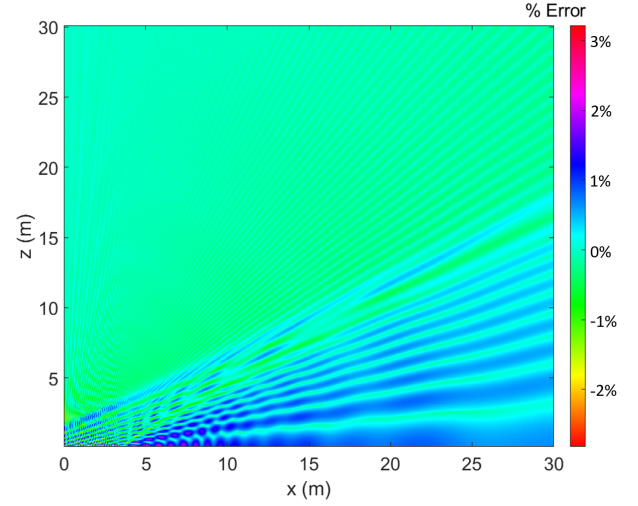


Fig. 5: Relative error (in percentage) of the AAL model with respect to the integral formulation of (16).

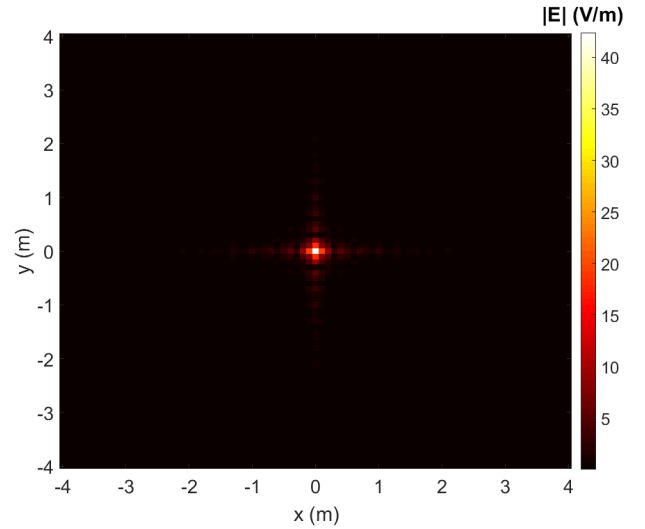


Fig. 6: Reradiated field [V/m] for a 7×7 m focalizing lens. Except for the phase profile of the metasurface, the setup is the same as for Fig. 4.

relative error is shown to be smaller than 1-2% for most of the observation domain. Therefore, both the considered versions of the model can be used but the AAL formulation is simpler and faster.

2) *Ideal Focalizing Lens*: the second canonical case study corresponds to an ideal, lossless metasurface with a single reradiated mode that focuses the incident wave towards a desired location, i.e., the metasurface is a focusing lens. The setup is the same as for the ideal anomalous reflector, with the difference that the angle of incidence is $\theta_i = 60$ degrees, the RIS lies in the xy plane at $z_0 = -10$ m, and the focusing spot is at the origin. Thus, the phase profile in (12) is set equal to $\chi_{m_1}(x', y') = k\sqrt{(x')^2 + (y')^2 + (z_0)^2} - k\sin\theta_i x'$. The results are illustrated in Fig. 6, where we see the focusing spot at the desired location. Also, we see that the electric field is approximately 40 times stronger than for the anomalous

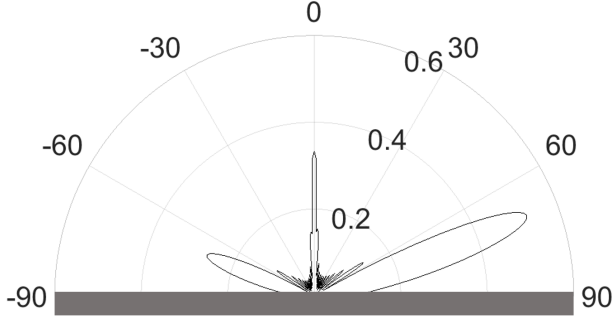


Fig. 7: Radiation pattern of the lossless anomalous reflector in [19]. Setup: normal incidence and the desired angle of reflection is 70 degrees.

reflector thanks to the focusing capability of the RIS.

3) *Lossless Anomalous Reflector (with parasitic modes)*: to further assess the model's capabilities we reproduced results of [19, Fig. 9], where the scattering pattern of a lossless, periodic, locally-designed phase-gradient RIS that generates anomalous reflection plus parasitic specular and symmetric reflection, is computed through both electromagnetic simulation and an approximate analytic method. The setup is the same as in [19] and corresponds to a metasurface that is illuminated with normal incidence by a plane wave at 3 GHz. The modulation period of the metasurface is $D=0.1064$ m and the size of the RIS is $10D \times 10D$. The reradiated field is evaluated at a distance equal to 22.64 m, which is close to the Fraunhofer far field boundary. The results are shown in Fig. 7. The radiation pattern in Fig. 7 is obtained by using the AAL formulation under the assumption of no losses and no diffuse scattering. In particular, the reradiated field in (26) is computed twice, once for each of the two anomalous re-radiation mode, and the result is combined with specular reflection and diffraction computed with a traditional, ray tracing approach. Finally, the different mechanisms are weighted according to the power-balance of equation (10) and summed coherently to get the overall field. More precisely, Fig. 7 is obtained by setting $\rho=0.17$ (undesired specular reflection), $m_1=0.76$ (desired anomalous reflection), and $m_2=0.17$ (undesired symmetric reflection). By comparing Fig. 7 with [19, Fig. 9], we observe a very good agreement between the two radiation patterns, which validates our approach.

4) *Modelling Diffuse Scattering*: the fourth case study is focused on the impact of diffuse scattering due to design or construction inaccuracies and/or dust deposit. To the best of our knowledge, no experimental results on the modeling of diffuse scattering from real-life engineered surfaces exist in the literature. Thus, we conduct a parametric study, in order to assess the potential impact of diffuse scattering on the radiation pattern of an RIS. The numerical results are shown in Fig. 8 for different values of S in (11).

The metasurface considered in Fig. 8 is the lossless anomalous reflector analyzed in the previous case study and illustrated in Fig. 7 in the absence of diffuse scattering. In Fig. 8, we see the impact of diffuse scattering under the assumption that 40% ($S^2=0.4$) or 80% ($S^2=0.8$) of the incident

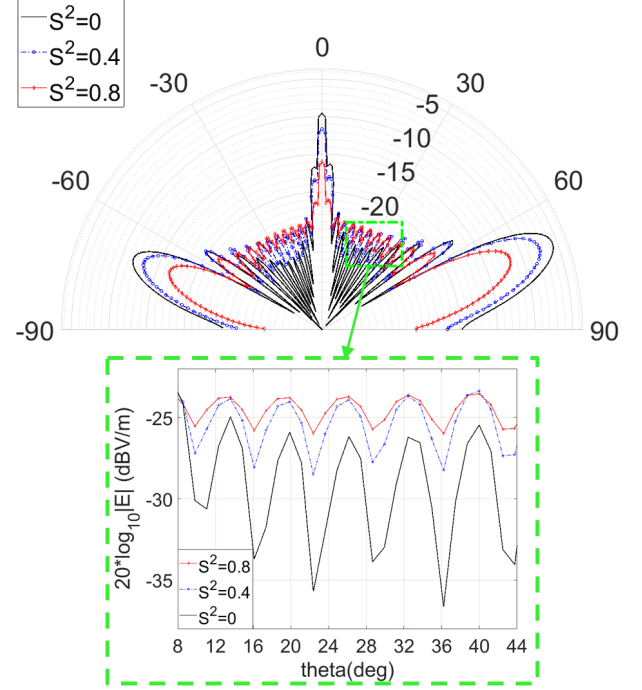


Fig. 8: Far-field (dBV/m) scattering pattern of the lossless anomalous reflector considered in [19] in the absence of diffuse scattering (reference black curve), with 40% (blue curve) and 80% (red curve) of the incident power diverted into diffuse scattering.

power is diverted into diffuse scattering according to the power conservation flow in (11). The ER approach with a Lambertian diffuse scattering pattern is used here in combination with the other mechanisms already considered in Fig. 7 and provided that power-balance (11) is satisfied. Although the considered S values are probably overestimated to amplify the scattering effect for the sake of figure legibility, nevertheless Fig. 8 shows the important role that diffuse scattering may play in RIS-assisted communications. In particular, we see a reduction of the intensity of the electric field towards the desired direction of reflection and an increase of the sidelobes as the scattering parameter S increases. Differently from Fig. 7, a logarithmic scale is used here to highlight the sidelobes. Part of the plot is also zoomed in (see green rectangle at the bottom of Fig. 8), to better highlight the influence of the S parameter on the reradiation sidelobes.

5) *Lossy Anomalous Reflector*: the fifth case study is focused on the validation of the proposed macroscopic model for characterizing a phase-gradient lossy metasurface that has been manufactured and studied with experimental measurements [29]. To match our model's parameters with the metasurface designed in [29], we set $\rho = 0$ and $S = 0$. In addition, the metasurface in [29] is designed to realize anomalous reflection and to suppress parasitic reradiation modes. As this metasurface is locally-designed, part of the incident power is dissipated. Therefore, a single reradiated mode exists and (11) reduces to $m + \tau = 1$. The rest of the simulation parameters are the same as those in [29]. The far field radiation pattern obtained with the AAL formulation is

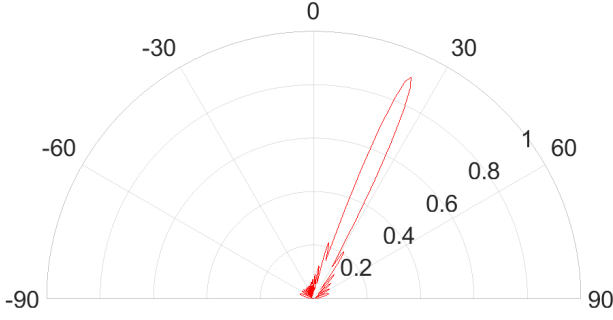


Fig. 9: Far-field radiation pattern ($\rho = 0, S = 0, m = 0.97$) corresponding to the lossy phase-gradient metasurface illustrated in [29, Fig 2.c]. The corresponding benchmark radiation pattern is in [29, Fig 2.d].

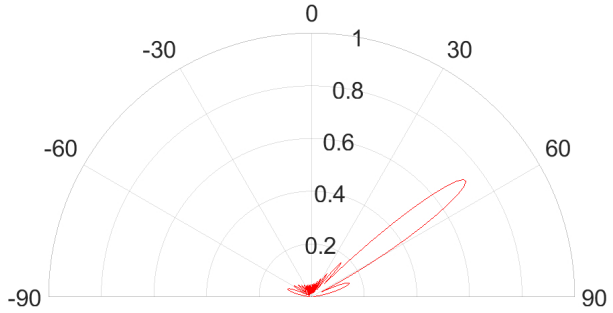


Fig. 10: Far-field radiation pattern ($\rho = 0, S = 0, m = 0.9$) corresponding to the lossy phase-gradient metasurface illustrated in [29, Fig 2.e]. The corresponding benchmark radiation pattern is in [29, Fig 2.f].

illustrated in Fig. 9 and Fig. 10 for two different angles of desired reflection.

From Fig. 9 and Fig. 10, which are obtained by setting $m = 0.97$ and $m = 0.9$, respectively, we see that the radiation patterns are in good agreement with those in [29]. This confirms the applicability of the proposed macroscopic reradiation and power conservation models even for experimentally characterized lossy metasurfaces.

6) *Analysis of the Spreading Factor*: the final case study is focused on evaluating the capability of the model to reproduce the correct near-field to far-field transition of the field scattered by a finite-size RIS. In the near field we have a plane wave with a spreading factor equal to 1 (Path Loss Exponent $\alpha=0$), while in the far field we must have a spherical wave ($\alpha=2$). To this end, we consider the same phase gradient anomalous reflector as in Fig. 4 and we compute local averages of the intensity of the electric field over spots of size $10\lambda \times 10\lambda$ as a function of the observation distance along the axis of the reradiation lobe from the center of the RIS. The results are shown in Fig. 11.

From Fig. 11, we see that the electric field intensity trend is consistent with the theory. In particular, we note that the average field remains almost constant in the near field region because of the large size of the RIS as compared to distance. Then, we observe some ripple effects, which are due to the impact of the edge-diffracted waves that is caused by the finite

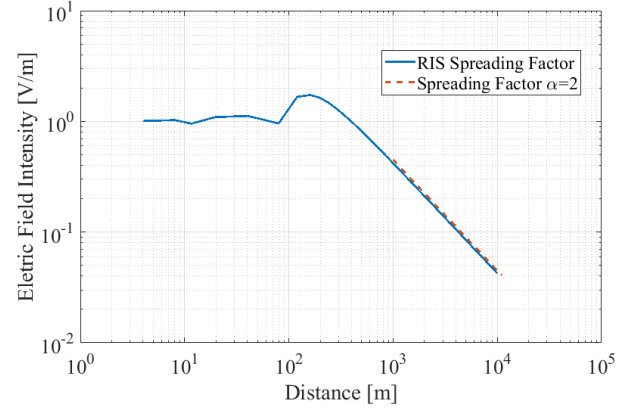


Fig. 11: Local average of the electric field amplitude computed from (16) as a function of the distance. The same setup as in Fig. 4 is used.

size of the RIS. As the distance increases, the intensity of the electric field converges towards a far-field spherical wave trend with $\alpha=2$ - as it should - beyond the Fraunhofer distance of 1000 m. Therefore, we conclude that the proposed approach well models both near field and far field propagation regimes.

V. CONCLUSION

In this paper, we have introduced a physically consistent macroscopic model for evaluating multi-mode reradiation and diffuse scattering from general reconfigurable engineered surfaces. The model is based on a hybrid approach where a well-established ray-based model to describe specular reflection, diffraction and diffuse scattering is married with a Huygens-based approach to describe anomalous reflection, and the two parts are kept together through a parametric power-balance formulation to satisfy the energy conservation principle. We have compared two different formulations of the Huygens-based approach: the first is based on the induction theorem and the second on antenna-array theory, and we have discussed their accuracy. In addition, we have implemented the overall macroscopic model and have validated its accuracy vs. analytical models, full-wave electromagnetic simulations, and experimental results available in the literature. Further work will deal with the use of the model within a ray tracing tool to perform link-level and system-level performance assessments in realistic multipath propagation scenarios, as well as with the development of a ray-based representation of multi-mode reradiation from the most important types of reconfigurable engineered surfaces.

APPENDIX A

DERIVATION OF FORMULA (16) FOR THE RERADIATED FIELD

By virtue of the induction theorem and the theorem of image currents [22], [23], the field reradiated by a physical object that is illuminated by an incident electromagnetic field can be determined by equivalent electric and magnetic current densities, which depend on the incident signal, and by appropriate image current densities, which depend on the incident signal and the

physical properties of the object, i.e., the RIS in our case. Usually, in canonical electromagnetic scattering problems the object is assumed to be either a PEC or a PMC. However, an RIS is a more complex surface, for which it is necessary to consider Maxwell's equations in the presence of both electric and magnetic currents and to derive the radiation field from both currents [19].

The method of current images can be generalized in the presence of an RIS as shown in Fig. A1. Fig. A1.a represents the conventional case of a PEC surface, where the induced electric currents are shorted by the PEC, and then after applying the method of images and removing the surface, only magnetic currents survive. On the other hand, Fig. A1.b depicts the case of a surface with generic surface impedance, and the RIS-modified method of images, where electric and magnetic currents are present after removing the surface, both depending on the macroscopic reflection coefficient Γ .

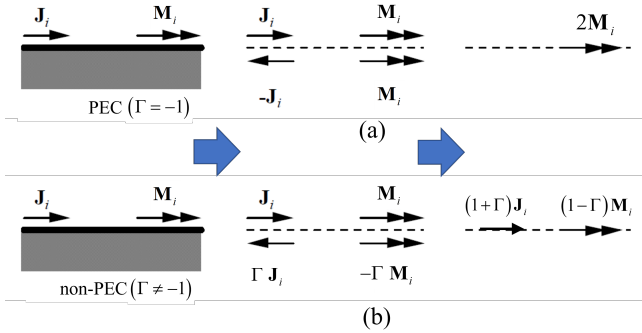


Fig. A1: Conventional (a) and modified (b) method of image currents: image currents replace the presence of the obstacle for the purpose of calculating the field outside of it.

In particular, according to the induction theorem the induced surface currents are:

$$\begin{aligned} \mathbf{J}_i(P') &= \mathbf{H}_i(P') \times \hat{\mathbf{n}} \\ \mathbf{M}_i(P') &= \hat{\mathbf{n}} \times \mathbf{E}_i(P') \end{aligned} \quad (\text{A.1})$$

where $P' = (x', y') \in S_{RIS}$ is the generic point on the surface of the RIS, $\hat{\mathbf{n}}$ is the normal vector that points outwards (i.e., towards the reflection half-space), and \mathbf{E}_i and \mathbf{H}_i are the incident electric and magnetic fields, respectively. In addition, the image current densities are (see Fig. A1.b):

$$\begin{aligned} \mathbf{J}_{\text{imag}}(P') &= \Gamma(P') \mathbf{J}_i(P') \\ \mathbf{M}_{\text{imag}}(P') &= -\Gamma(P') \mathbf{M}_i(P') \end{aligned} \quad (\text{A.2})$$

where $\Gamma(P')$ is the macroscopic reflection coefficient in (12).

Based on (A.1) and (A.2), the reradiation of the RIS can be calculated by replacing the RIS with the total surface current densities as follows:

$$\begin{aligned} \mathbf{J}(P') &= (1 + \Gamma(P')) [\mathbf{H}_i(P') \times \hat{\mathbf{n}}] \\ \mathbf{M}(P') &= (1 - \Gamma(P')) [\hat{\mathbf{n}} \times \mathbf{E}_i(P')] \end{aligned} \quad (\text{A.3})$$

and by assuming that the reradiation occurs in the absence of any physical objects, i.e., in free space.

The total surface currents in (A.3) assume that the RIS is of infinite extent and the impact of the edge effects on the

surface current densities is ignored. By using the notation in Fig. 3, the electric field that is reradiated by a finite-size RIS can be obtained from Kottler's formula [[30], Eq. (18.4.1)]:

$$\begin{aligned} \mathbf{E}_m(P) &= 1/(j\omega\epsilon) \int \int_{S_{RIS}} k^2 G(x', y') \mathbf{J}(x', y') dS \\ &+ 1/(j\omega\epsilon) \int \int_{S_{RIS}} (\mathbf{J}(x', y') \cdot \nabla') \nabla' G(x', y') dS \\ &- 1/(j\omega\epsilon) \int \int_{S_{RIS}} j\omega\epsilon \mathbf{M}(x', y') \times \nabla' G(x', y') dS \end{aligned} \quad (\text{A.4})$$

where ∇' denotes the gradient with respect to (x', y') , " \cdot " denotes the dot scalar product, " \times " denotes the vector product, " \cdot " denotes the dot scalar product, and $G(x', y')$ is the Green function in free space:

$$G(x', y') = e^{-jk|\mathbf{r}-\mathbf{r}'|} / (4\pi|\mathbf{r}-\mathbf{r}'|) = e^{-jk r''} / (4\pi r'') \quad (\text{A.5})$$

where $\mathbf{r}'' = \mathbf{r} - \mathbf{r}'$ and $r'' = |\mathbf{r}''|$.

The second integral in (A.4) can be simplified by taking into account that, for typical communication scenarios that encompass the radiative near and far field of the RIS (excluding then the reactive near field region), the approximation $jk + 1/|\mathbf{r}-\mathbf{r}'| \approx jk$ holds true, which implies $\nabla' G(x', y') \approx jk \hat{\mathbf{r}}''$, where $\hat{\mathbf{r}}'' = \mathbf{r}''/|\mathbf{r}''|$. Under these assumptions, the following approximations hold true:

$$\begin{aligned} \partial/\partial x' (G(x', y') \hat{\mathbf{r}}'') &\approx jk G(x', y') (x - x') \hat{\mathbf{r}}'' / r'' \\ \partial/\partial y' (G(x', y') \hat{\mathbf{r}}'') &\approx jk G(x', y') (y - y') \hat{\mathbf{r}}'' / r'' \end{aligned} \quad (\text{A.6})$$

By using (A.6), the following approximation is obtained:

$$\begin{aligned} (\mathbf{J}(x', y') \cdot \nabla') \nabla' G(x', y') \\ \approx (jk)^2 G(x', y') (\mathbf{J}(x', y') \cdot \hat{\mathbf{r}}'') \hat{\mathbf{r}}'' \end{aligned} \quad (\text{A.7})$$

Also, the following triple vector product identity holds:

$$\begin{aligned} \mathbf{J}(x', y') - (\mathbf{J}(x', y') \cdot \hat{\mathbf{r}}'') \hat{\mathbf{r}}'' \\ \approx \hat{\mathbf{r}}'' \times (\mathbf{J}(x', y') \times \hat{\mathbf{r}}'') \end{aligned} \quad (\text{A.8})$$

Finally, by inserting (A.6) and (A.7) in (A.4), the reradiated electric field can be formulated as follows:

$$\begin{aligned} \mathbf{E}_m(P) &\approx \\ &-jk \int \int_{S_{RIS}} \eta G(x', y') [\hat{\mathbf{r}}'' \times (\mathbf{J}(x', y') \times \hat{\mathbf{r}}'')] dS \\ &-jk \int \int_{S_{RIS}} \eta G(x', y') (\mathbf{M}(x', y') \times \hat{\mathbf{r}}'') dS \end{aligned} \quad (\text{A.9})$$

By substituting (A.3) and (A.5) in (A.9), we eventually obtain (16). The proof follows by noting that the reradiated field in (A.9) is formulated in terms of the surface current densities in (A.3) and, therefore, it can be obtained from the incident signal and the macroscopic reflection coefficient in (12).

Finally, we note that (A.9) may be simplified and, in some cases, may be formulated in a closed-form expression in the Fraunhofer far field of the RIS. Due to space limitations, the corresponding formula is not reported but it may be obtained by using the following approximation:

$$G(x', y') = \frac{e^{-jk|\mathbf{r}-\mathbf{r}'|}}{4\pi|\mathbf{r}-\mathbf{r}'|} \approx \frac{e^{-jk|\mathbf{r}|}}{4\pi|\mathbf{r}|} \exp\left(jk \left(\frac{\mathbf{r}}{|\mathbf{r}|} \cdot \mathbf{r}'\right)\right) \quad (\text{A.10})$$

REFERENCES

- [1] M. Di Renzo et al., "Smart radio environments empowered by reconfigurable AI meta-surfaces: An idea whose time has come," *EURASIP J. Wireless Commun. Netw.*, vol. 2019, Dec. 2019.
- [2] E. Basar et al., "Wireless communications through reconfigurable intelligent surfaces," *IEEE Access*, vol. 7, pp. 116753–116773, 2019.
- [3] C. Huang et al., "Holographic MIMO surfaces for 6G wireless networks: Opportunities, challenges, and trends," vol. 17, no. 5, pp. 118–125, Oct. 2020.
- [4] Q. Wu and R. Zhang, "Towards smart and reconfigurable environment: Intelligent reflecting surface aided wireless network," *IEEE Commun. Mag.*, vol. 58, no. 1, pp. 106–112, Jan. 2020.
- [5] M. Di Renzo et al., "Smart radio environments empowered by reconfigurable intelligent surfaces: How it works, state of research, and the road ahead," *IEEE J. Sel. Areas Commun.*, vol. 38, no. 11, pp. 2450–2525, Nov. 2020.
- [6] Q. Wu, S. Zhang, B. Zheng, C. You and R. Zhang, "Intelligent Reflecting Surface-Aided Wireless Communications: A Tutorial," *IEEE Trans. Commun.*, vol. 69, no. 5, pp. 3313–3351, May 2021.
- [7] M. Di Renzo et al., "Reconfigurable intelligent surfaces vs. Relaying: Differences, similarities, and performance comparison," *IEEE Open J. Commun. Society*, vol. 1, pp. 798–807, 2020.
- [8] M. Di Renzo, F. H. Danufane, X. Xi, J. de Rosny, and S. Tretyakov, "Analytical modeling of the path-loss for reconfigurable intelligent surfaces - Anomalous mirror or scatterer?" *IEEE Int. Workshop Signal Process. Adv. Wireless Commun. (SPAWC)*, May 2020, pp. 1–5.
- [9] W. Tang et al., "Wireless communications with reconfigurable intelligent surface: Path loss modeling and experimental measurement," *IEEE Trans. Wireless Commun.*, vol. 20, no. 1, pp. 421–439, Jan. 2021.
- [10] W. Tang et al., "Path loss modeling and measurements for reconfigurable intelligent surfaces in the millimeter-wave frequency band," 2021. [Online]. Available: <http://arxiv.org/abs/2101.08607>.
- [11] S. W. Ellingson, "Path loss in reconfigurable intelligent surface-enabled channels", 2019. [Online]. Available: <https://arxiv.org/pdf/1912.06759.pdf>.
- [12] O. Ozdogan, E. Bjornson, and E. G. Larsson, "Intelligent reflecting surfaces: Physics, propagation, and pathloss modeling," *IEEE Wireless Commun. Lett.*, vol. 9, no. 5, pp. 581–585, May 2020.
- [13] J. C. B. Garcia, A. Sibille, and M. Kamoun, "Reconfigurable intelligent surfaces: Bridging the gap between scattering and reflection," *IEEE J. Sel. Areas Commun.*, vol. 38, no. 11, pp. 2538–2547, Nov. 2020.
- [14] M. Najafi, V. Jamali, R. Schober, H. V. Poor, "Physics-based modeling and scalable optimization of large intelligent reflecting surfaces," *IEEE Trans. Commun.*, vol. 69, no. 4, pp. 2673–2691, Apr. 2021.
- [15] G. Gradoni and M. Di Renzo, "End-to-end mutual coupling aware communication model for reconfigurable intelligent surfaces: An electromagnetic-compliant approach based on mutual impedances," *IEEE Wireless Commun. Lett.*, vol. 10, no. 5, pp. 938–942, May 2021.
- [16] X. Qian and M. Di Renzo, "Mutual coupling and unit cell aware optimization for reconfigurable intelligent surfaces," *IEEE Wireless Commun. Lett.*, vol. 10, no. 6, pp. 1183–1187, June 2021.
- [17] A. Abrardo et al. "MIMO interference channels assisted by reconfigurable intelligent surfaces: Mutual coupling aware sum-rate optimization based on a mutual impedance channel model", 2021. [Online]. Available: <https://arxiv.org/pdf/2102.07155.pdf>.
- [18] F. H. Danufane, M. Di Renzo, J. de Rosny, and S. Tretyakov, "On the path-loss of reconfigurable intelligent surfaces: An approach based on Green's theorem applied to vector fields," *IEEE Trans. Commun.*, *IEEE Early Access* (10.1109/TCOMM.2021.3081452), 2021.
- [19] A. Diaz-Rubio and S. A. Tretyakov, "Macroscopic modeling of anomalously reflecting metasurfaces: Angular response and far-field scattering," *IEEE Trans. Antennas Propag.*, *IEEE Early Access* (10.1109/TAP.2021.3076267), 2021.
- [20] V. Degli-Esposti, F. Fuschini, E. Vitucci, G. Falciasecce, "Measurement and modelling of scattering from buildings", *IEEE Trans. Antennas Propag.*, vol. 55 no 1, pp. 143–153, Jan. 2007.
- [21] F. Fuschini, E. M. Vitucci, M. Barbiroli, G. Falciasecce, V. Degli-Esposti, "Ray tracing propagation modeling for future small-cell and indoor applications: a review of current techniques", *Radio Science*, vol. 50, no. 6, pp. 469–485, June 2015.
- [22] C. Balanis, "Advanced Engineering Electromagnetics", Wiley, 1989.
- [23] C. Balanis, "Antenna Theory: Analysis and Design", Wiley, 2016.
- [24] J. S. Lu, E. M. Vitucci, V. Degli-Esposti, F. Fuschini, M. Barbiroli, J. Blaha, H. L. Bertoni, "A discrete environment-driven GPU-based ray launching algorithm", *IEEE Trans. Antennas Propag.*, vol. 67 no. 02, pp. 1558–2221, Feb. 2019.
- [25] A. Diaz-Rubio, V. S. Asadchy, A. Elsakka, and S. A. Tretyakov, "From the generalized reflection law to the realization of perfect anomalous reflectors", *Science Advances*, vol. 3, no. 8, e1602714, 2017.
- [26] F. Fuschini, V. Degli-Esposti, and E. M. Vitucci, "A model for forward-diffuse scattering through a wall," *4th European Conf. Antennas Propag.*, Barcelona, Spain, 12–16 Apr. 2010.
- [27] B. Zhu, L. Zhao, and Y. Feng, "Active impedance metasurface with full 360° reflection phase tuning", *Sci. Rep.* 3, 3059, 2013.
- [28] P.-S. Kildal, "Foundations of Antenna Engineering: A Unified Approach for Line-of-Sight and Multipath", Kildal Foundation, March 2021. Available at: <https://www.kildal.se/downloads/>.
- [29] S. Shulin, H. Qiong, X. Shiyi, X. Qin, L. Xin and Z. Lei, "Gradient-index meta-surfaces as a bridge linking propagating waves and surface waves", *Nature Materials*, 11, 426–31, 2012.
- [30] S. J. Orfanidis, "Electromagnetic Waves and Antennas". Available at: <https://www.ece.rutgers.edu/~orfanidi/ewa/>.